Article

Structure-based classification of tauopathies

Yang Shi[1,14], Wenjuan Zhang[1,14], Yang Yang[1], Alexey G. Murzin[1], Benjamin Falcon[1], Abhay Kotecha[2], Mike van Beers[2], Airi Tarutani[3], Fuyuki Kametani[3], Holly J. Garringer[4], Ruben Vidal[4], Grace I. Hallinan[4], Tammaryn Lashley[5], Yuko Saito[6], Shigeo Murayama[7], Mari Yoshida[8], Hidetomo Tanaka[9], Akiyoshi Kakita[9], Takeshi Ikeuchi[10], Andrew C. Robinson[11], David M. A. Mann[11], Gabor G. Kovacs[12,13], Tamas Revesz[5], Bernardino Ghetti[4], Masato Hasegawa[3], Michel Goedert[1,15] ✉ & Sjors H. W. Scheres[1,15] ✉
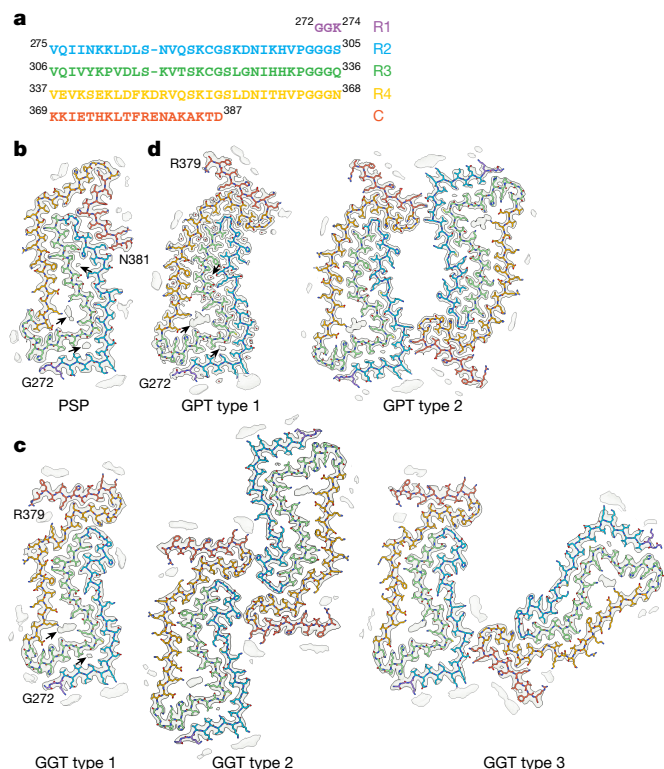
The ordered assembly of tau protein into filaments characterizes several neurodegenerative diseases, which are called tauopathies. It was previously reported that, by cryo-electron microscopy, the structures of tau filaments from Alzheimer's disease[1,2], Pick's disease[3], chronic traumatic encephalopathy[4] and corticobasal degeneration[5] are distinct. Here we show that the structures of tau filaments from progressive supranuclear palsy (PSP) define a new three-layered fold. Moreover, the structures of tau filaments from globular glial tauopathy are similar to those from PSP. The tau filament fold of argyrophilic grain disease (AGD) differs, instead resembling the four-layered fold of corticobasal degeneration. The AGD fold is also observed in ageing-related tau astrogliopathy. Tau protofilament structures from inherited cases of mutations at positions +3 or +16 in intron 10 of *MAPT* (the microtubule-associated protein tau gene) are also identical to those from AGD, suggesting that relative overproduction of four-repeat tau can give rise to the AGD fold. Finally, the structures of tau filaments from cases of familial British dementia and familial Danish dementia are the same as those from cases of Alzheimer's disease and primary age-related tauopathy. These findings suggest a hierarchical classification of tauopathies on the basis of their filament folds, which complements clinical diagnosis and neuropathology and also allows the identification of new entities—as we show for a case diagnosed as PSP, but with filament structures that are intermediate between those of globular glial tauopathy and PSP.

Six tau isoforms are expressed in the adult human brain; three isoforms have three microtubule-binding repeats (3R) and three isoforms have four repeats (4R)[6]. On the basis of the isoforms that constitute the abnormal filaments, tauopathies can be divided into three groups. In primary age-related tauopathy (PART), Alzheimer's disease, familial British dementia (FBD), familial Danish dementia (FDD) and chronic traumatic encephalopathy (CTE), a mixture of 3R and 4R tau isoforms is present in the filaments; 3R tau is found in Pick's disease, whereas 4R tau isoforms are present in the filaments of PSP, globular glial tauopathy (GGT), corticobasal degeneration (CBD), AGD and ageing-related tau astrogliopathy (ARTAG). Dominantly inherited mutations in *MAPT* cause frontotemporal dementias, with filaments made of 3R, 4R or both 3R and 4R (3R+4R) tau isoforms[7].

It was previously shown that Alzheimer's disease, CTE, Pick's disease and CBD are each characterized by a different tau fold[1–5], whereas PART filaments are identical to those from Alzheimer's disease[8]. To expand our knowledge of tau filaments in disease, we determined the cryo-electron microscopy (cryo-EM) structures of tau filaments from the brains of individuals with typical and atypical PSP, GGT, AGD, ARTAG and *MAPT* intron-10 mutations +3 and +16, as well as individuals with FBD and FDD (Extended Data Figs. 1–4, Extended Data Tables 1, 2, Supplementary Tables 1–3).

First, we examined filaments from PSP, which is the most common tauopathy after Alzheimer's disease and belongs to the group of sporadic frontotemporal lobar degeneration disorders (FTLD-tau). Clinically, typical cases of PSP (Richardson's syndrome; PSP-RS) are

[1]MRC Laboratory of Molecular Biology, Cambridge, UK. [2]Thermo Fisher Scientific, Eindhoven, The Netherlands. [3]Department of Brain and Neurosciences, Tokyo Metropolitan Institute of Medical Science, Tokyo, Japan. [4]Department of Pathology and Laboratory Medicine, Indiana University School of Medicine, Indianapolis, IN, USA. [5]Department of Neurodegenerative Disease and Queen Square Brain Bank for Neurological Disorders, UCL Queen Square Institute of Neurology, London, UK. [6]Department of Neuropathology, Tokyo Metropolitan Geriatric Hospital and Institute of Gerontology, Tokyo, Japan. [7]Molecular Research Center for Children's Mental Development, United Graduate School of Child Development, University of Osaka, Osaka, Japan. [8]Institute for Medical Science of Aging, Aichi Medical University, Nagakute, Japan. [9]Department of Pathology, Brain Research Institute, Niigata University, Niigata, Japan. [10]Department of Molecular Genetics, Brain Research Institute, Niigata University, Niigata, Japan. [11]Clinical Sciences Building, University of Manchester, Salford Royal Foundation Trust, Salford, UK. [12]Department of Laboratory Medicine and Pathobiology and Tanz Centre for Research in Neurodegenerative Diseases, University of Toronto, Toronto, Ontario, Canada. [13]Institute of Neurology, Medical University of Vienna, Vienna, Austria. [14]These authors contributed equally: Yang Shi, Wenjuan Zhang. [15]These authors jointly supervised this work: Michel Goedert, Sjors H. W. Scheres. ✉e-mail: mg@mrc-lmb.cam.ac.uk; scheres@mrc-lmb.cam.ac.uk

a

	272GGK274	R1
275VQIINKKLDLS-NVQSKCGSKDNIKHVPGGGS305		R2
306VQIVYKPVDLS-KVTSKCGSLGNIHHKPGGGQ336		R3
337VEVKSEKLDFKDRVQSKIGSLDNITHVPGGGN368		R4
369KKIETHKLTFRENAKAKTD387		C

Fig. 1 | Three-layered 4R tau filament structures. a, Amino acid sequence of tau residues 272–387. Residues in R1–R4 and in the C-terminal domain are coloured purple, blue, green, gold and orange, respectively. **b**, Cryo-EM density map (in transparent grey) and atomic model for the PSP filaments. **c**, As in **b**, for GGT type 1, GGT type 2 and GGT type 3 filaments. **d**, As in **b**, for GPT type 1 and GPT type 2 filaments. Black arrows point to additional densities that are described in the main text.

characterized by postural instability, supranuclear gaze palsy, behavioural and cognitive impairment, as well as bulbar symptoms[9,10]. Neuropathologically, they are defined by abundant subcortical neurofibrillary tangles and neuropil threads, together with tufted astrocytes and oligodendroglial coiled bodies[11,12]. Atypical forms of PSP are distinguished by differences in total tau load in specific brain regions[12]. We determined structures—with resolutions of up to 2.7 Å—of tau filaments from the frontal cortex and thalamus of three individuals with PSP-RS, the putamen and temporal cortex of two individuals with PSP with predominant frontal presentation (PSP-F), the frontal cortex of one individual with predominant parkinsonism (PSP-P) and the frontal cortex of one individual with a predominant presentation of corticobasal syndrome (PSP-CBS).

In PSP-RS, PSP-CBS, PSP-P and the first case of PSP-F, we observed tau filaments made of a single protofilament with an ordered core that spans residues 272–381. Although this is essentially the same region as that seen in the CBD core, it adopts a markedly different conformation, which we named the PSP fold (Fig. 1b, Extended Data Fig. 4a). Tau filament structures were identical between typical and atypical cases of PSP, consistent with the view that the initiating sites of tau pathology are similar in clinical subtypes, which are distinguished by different propagation patterns. When multiple tau seeds are found in the brain of an individual with PSP[13], this may be indicative of co-pathology.

In the PSP fold, repeats 2–4 (R2–4) form a three-layer meander that turns at the conserved PGGG motifs at the end of each repeat. R3 forms the central layer, which bends at G323 into a near-right angle. Following the outside of this bend, R2 packs against the entirety of R3. The R2–R3 interface contains two small cavities that include additional densities. One, between N279 and G323, and surrounded by hydrophobic side

chains, is probably caused by molecules of a predominantly non-polar nature, whereas the other, next to the salt bridge between K294 and D314, is most likely to be a solvent molecule. Most of R4 packs against the other side of R3. At the R3–R4 interface, there is a cavity between the positively charged K317, K321 and K340 that contains a bigger additional density, with a volume of around 30 Å[3], which presumably corresponds to anionic molecules. This cavity is flanked by the negatively charged E338 and E342, reducing the net charge of the cavity to +1 per rung. The rest of the R3–R4 interface is of a mixed chemical nature, containing hydrophobic interactions and a salt bridge between K311 and D348. The chain makes another hairpin turn at the PGGG motif of R4, with the C-terminal segment forming a short fourth layer that covers the end of R2. On the outside of the PSP core, there are at least six additional densities that were conserved between cases, the most prominent being next to K280–K281 and H362.

We then examined tau filaments from GGT. Like PSP, GGT is a sporadic 4R tauopathy that belongs to the spectrum of FTLD-tau diseases; it is characterized by abundant globular glial tau inclusions[14–16]. GGT is divided into three types (GGT-I, GGT-II and GGT-III), depending on the predominant involvement of glial cells in white or grey matter. Structures of tau filaments from the frontal cortex of previously described cases of GGT-I (case 1 in ref. [17]) and GGT-II (case 1 in ref. [18]), with resolutions of up to 2.9 Å, show a common three-layered protofilament fold that was—to our knowledge—previously unknown, which spans residues 272–379 (Fig. 1c, Extended Data Fig. 4b). For GGT-I, we observed three types of filament: type 1 comprises a single protofilament with the GGT fold; type 2 packs two protofilaments with approximate 2₁ screw symmetry; and type 3 packs two protofilaments in an asymmetrical manner. For GGT-II, we only observed filaments of types 2 and 3. We were unable to solve the structures of tau filaments from the frontal cortex of a previously described case of GGT-III (case 1 in ref. [19]), because of an absence of twist in the imaged filaments.

The GGT fold comprises essentially the same residues as the PSP fold and has a similar three-layered arrangement of R2–4. Again, the chain turns at the PGGG motifs, but each turn has a different conformation compared to its PSP counterpart. Moreover, the C-terminal domain points in the opposite direction and packs against the end of R4 in a hairpin-like structure that is almost identical to the equivalent part of the Pick fold. The only common substructure of the GGT and PSP folds comprises residues 273–285 and 322–330, extending to the additional densities in the small internal cavity between N279 and G323 and outside K280–K281. The cavity at the R3–R4 interface is bigger in the GGT than in the PSP fold and it contains a larger non-proteinaceous density, with a volume of around 50 Å[3], surrounded by K317, K321 and K340. The net positive charge of the cavity is also greater, as E338 forms a salt bridge with K331.

Although the structures of tau filaments from the six cases of typical and atypical PSP described above were identical, we observed a different tau fold for filaments from the temporal cortex of the second individual with PSP-F (PSP-F case 2) (Fig. 1d, Extended Data Fig. 4c). As this fold resembled both the GGT and the PSP folds, we named it the GGT-PSP-Tau, or GPT, fold. We observed two types of GPT filament: type 1 filaments comprise a single protofilament; and type 2 filaments pack two protofilaments with approximate 2₁ screw symmetry, creating a large, solvent-filled cavity. Histologically, PSP-F case 2 was different from other cases of PSP: this case resembled cases with abundant spherical, 4R tau-immunoreactive, basophilic neuronal inclusions in limbic and other brain regions[20–22] (Extended Data Fig. 5).

For PSP-F case 2, we used the same electron microscope that was used previously for structure determination to atomic resolution of an apoferritin test sample[23]. Images from this microscope allowed classification into two alternative main-chain conformations, one of which led to a reconstruction with a resolution of 1.9 Å (Extended Data Fig. 6). This map allowed us to model 19 ordered water molecules per asymmetric unit, but it did not provide further insights into the nature of the
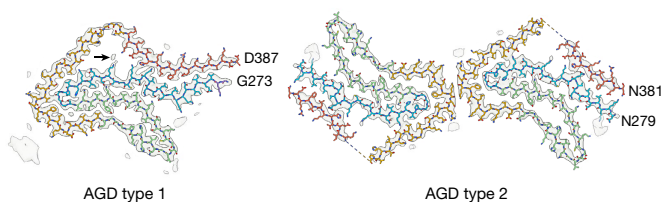
Fig. 2 | Four-layered 4R tau filament structures. Cryo-EM density map and atomic model for AGD type 1 filaments and AGD type 2 filaments. Colours are as in Fig. 1. The black arrow points to additional density discussed in the main text. The dotted lines indicate main chain connectivity for which cryo-EM density is missing.

constituent molecules of the additional densities, probably because they did not follow the helical symmetry.

The GPT fold comprises the same residues as the PSP and GGT folds and has a similar three-layered structure. The GPT fold has two large substructures of closely similar conformations compared to the GGT fold: the hairpin formed by residues 356–378, as well as residues 273–294 and 312–346, including the small and large cavities with their associated internal and external additional densities. The relative orientation of the two substructures differs between the GPT and the GGT folds, with different conformations of intervening sequences, in particular in the PGGG turn at the end of R2 and in the N-terminal part of R3 that have similar side-chain orientations to PSP. In GPT type 2 filaments, the two symmetric inter-protofilament interfaces resemble the asymmetric interface of GGT type 3 filaments, increasing the overall similarity between GGT and GPT filaments (Extended Data Fig. 6).

AGD is another 4R tauopathy that belongs to the spectrum of sporadic FTLD-tau diseases[24–28]. A defining feature is the presence of argyrophilic grains. Argyrophilic grains are rarely the sole pathological finding in individuals who are cognitively impaired, and are most commonly found together with other tau pathologies, especially neurofibrillary tangles[26]. We determined the structures of tau filaments from the nucleus accumbens of two individuals with AGD, with resolutions of up to 3.4 Å (Fig. 2, Extended Data Fig. 4d). We observed three types of filament with a common protofilament core—the AGD fold—that adopts a four-layered ordered structure comprising residues 273–387 (type 1) or 279–381 (type 2), and resembles the CBD fold[5]. Like CBD type I and type II filaments, AGD type 1 filaments comprise a single protofilament and AGD type 2 filaments pack two protofilaments with C2 symmetry. We were unable to solve the structure of AGD type 3 filaments to sufficient resolution for atomic modelling, but low-resolution cross-sections suggest an asymmetric packing of two protofilaments with the AGD fold. AGD case 1 also had the paired helical filaments (PHFs) that are found in Alzheimer's disease, and CTE type I filaments; AGD case 2 also had Alzheimer PHFs and straight filaments (Extended Data Fig. 2d).

Residues 293–357 of the AGD fold adopt the same conformation as in the CBD fold. However, the C-terminal segment (368–386) makes different interactions with R2, and the ordered core of the AGD fold is seven amino acids longer than that of the CBD fold. In addition, compared to the CBD cavity, the AGD cavity between R2 and the C-terminal segment is smaller and its net positive charge is less. It also contains a smaller additional density of unknown identity between K294 and K370. In AGD type 2 filaments, the turn at the end of R4, as well as the first and last six residues that form the ordered core of the AGD type 1 filaments, are disordered, and the termini point in a different direction compared to the AGD type 1 filaments.

Histologically, PSP-RS case 3 also had features of AGD, in particular the presence of argyrophilic grains in the entorhinal cortex (Extended Data Fig. 7). Consistent with this, besides filaments with the PSP fold

in thalamus, we also observed filaments of AGD type 2 and AGD type 3, as well as a minority of Alzheimer PHFs and straight filaments, in the entorhinal cortex of the PSP-RS case 3 (Extended Data Fig. 2e). By immunoblotting, the pattern of C-terminally truncated tau bands was like that of PSP in thalamus and like that of CBD in entorhinal cortex (Extended Data Fig. 8). Thus, this individual had concomitant PSP and AGD, as has been reported for other cases of PSP[26].

Astroglial 4R tau pathology in ageing has been increasingly recognized, and these cases have been subsumed under the umbrella term of ARTAG[29]. Like AGD, ARTAG usually coexists with other pathologies. Structures of the majority species of tau filaments from the hippocampus of an individual with ARTAG[30] were identical to those of AGD type 2 and type 3 filaments. Alzheimer PHFs and straight filaments were also observed (Extended Data Fig. 2f).

Unlike the sporadic diseases described above, mutations +3 and +16 in intron 10 of *MAPT* give rise to a 4R tauopathy that belongs to the spectrum of inherited FTLD-tau[31–34]. It is characterized by abundant filamentous tau inclusions in nerve cells and glial cells. Argyrophilic grains are present in the entorhinal cortex, hippocampus and frontal cortex. Structures of tau filaments from the frontal cortex of two individuals with the +3 mutation and one individual with the +16 mutation all showed the AGD fold (Extended Data Fig. 2g).

The differences between the structures of tau filaments from 4R tauopathies are consistent with results from immunoblots of sarkosyl-insoluble tau (Extended Data Fig. 8). In cases of PSP, CBD, GGT, AGD, ARTAG and *MAPT* intron-10 mutations +3 and +16, tau bands of 64 and 68 kDa were in evidence, indicating the presence of full-length 4R tau. As reported previously[35–37], a strong C-terminal tau band of 33 kDa was also found in PSP and GGT, whereas a strong tau doublet of 37 kDa was seen in CBD, AGD and cases with mutation +16. The 37-kDa bands were also characteristic of ARTAG and cases with mutation +3. The 33- and 37-kDa bands correspond to N-terminally truncated tau at, or near, residues 186–187 and 168–169, respectively. Assembled full-length tau is probably cleaved in the fuzzy coat, with the size differences between the 33-kDa and the 37-kDa bands possibly resulting from different arrangements of the ends of the structured cores.

Whereas all diseases described above are 4R tauopathies, we also determined structures of tau filaments from two inherited types of 3R+4R tauopathies. FBD and FDD are caused by mutations in the integral membrane protein 2B gene (*ITM2B*) and are characterized by many extracellular inclusions of British amyloid and Danish amyloid that are associated with abundant tau-positive neurofibrillary tangles, neuropil threads and dystrophic neurites[38–41]. Structures of tau filaments from the hippocampus of an individual with FBD (described in a previous study[40]) and the temporal cortex of an individual with FDD (Extended Data Fig. 2h) are identical to the PHFs that were previously observed for PART and Alzheimer's disease[1,2,8]. The hippocampus from the case of FBD also contained Alzheimer straight filaments, as well as CTE type I tau filaments, possibly as a result of head trauma.

Discussion

Clinical features are used to distinguish tauopathies. This is complemented and extended by post-mortem neuropathological examination. We now add a third layer of knowledge in the characterization of these diseases. The cryo-EM structures presented here, together with those described previously[1–5,8], provide an overarching perspective that suggests a hierarchical classification of tauopathies on the basis of their filament folds (Fig. 3). It was previously postulated that distinct conformers of filamentous tau define different tauopathies[5]. This observation still holds. We now also show that some tauopathies share the same fold, and that multiple levels of similarity exist between folds.

The first level of classification is based on the extent of the ordered cores, and coincides with the isoform compositions of tau inclusions in the corresponding diseases. All known tau folds from human diseases have a common ordered core region that comprises R3 and R4, as well
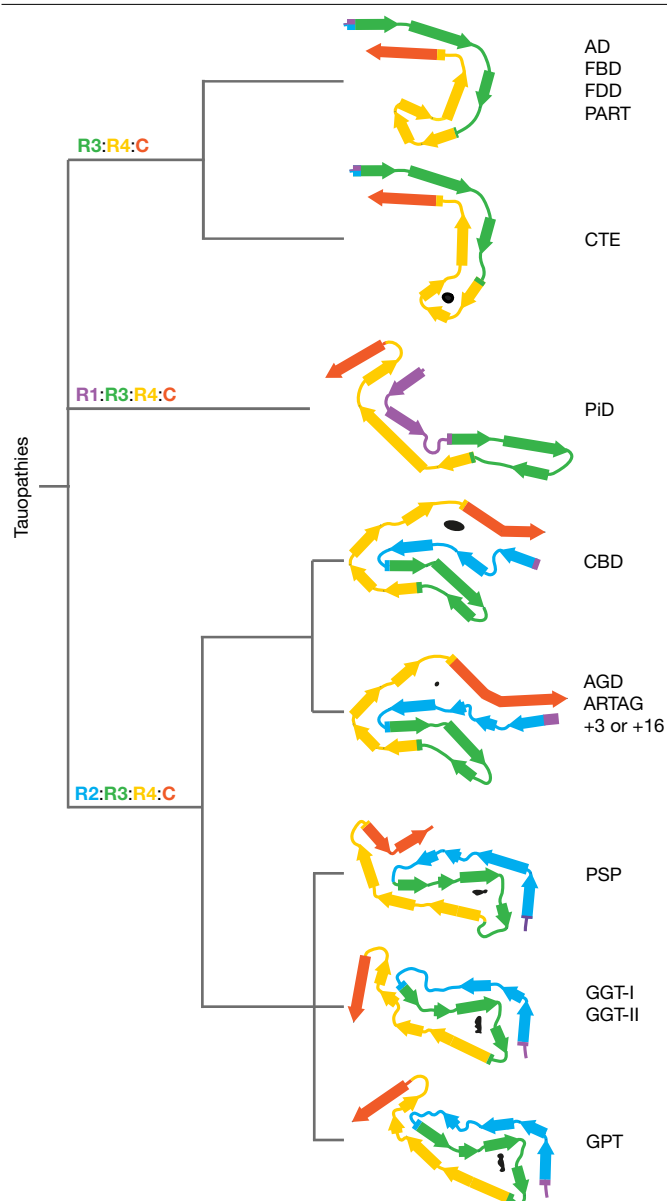
Fig. 3 | Structure-based classification of tauopathies. The dendrogram shows the proposed classification of tauopathies as described in the main text, with the corresponding folds displayed with the first β-strand in R3 oriented horizontally, except for the GGT and GPT folds, which are aligned to the PSP fold. Colours are as in Fig. 1. Internal, non-proteinaceous densities are shown in black. AD, Alzheimer's disease; PiD, Pick's disease.

as 10–13 amino acids of the C-terminal domain. However, the folds differ in their N-terminal extensions. The Alzheimer and CTE folds, which represent 3R+4R tauopathies, comprise only one or two amino acids from the C termini of R1 and R2. The Pick fold, which represents the only 3R tauopathy with known filament structures, comprises more than half of R1. Folds observed for 4R tauopathies comprise all of R2 and one or two residues of R1. As we previously observed for the CBD fold, the incorporation of 3R tau isoforms is incompatible with the PSP, GPT, GGT and AGD folds, which agrees with the observation that only 4R tau isoforms assemble in these diseases. The presence of N279 from R2 in the fuzzy coat of the Alzheimer fold may explain why this residue is deamidated in tau assemblies from Alzheimer's disease, but not in those from PSP or CBD[42].

At a second level, for the 3R+4R tauopathies, the CTE fold is distinct from the Alzheimer fold. However, whereas Alzheimer's disease, FBD

and FDD are distinct diseases that are characterized by different symptoms and/or neuropathology, they contain tau filaments with the Alzheimer fold. As exemplified by PART, which may be part of Alzheimer's disease[43], the Alzheimer tau fold can form in the absence of β-amyloid deposits. By contrast, in cases of Alzheimer's disease, FBD and FDD, the presence of extracellular amyloid deposits is accompanied by abundant intraneuronal tau inclusions with the Alzheimer fold. The Alzheimer fold has also recently been described in cases of prion disease with mutations Q160X and F198S in the *PRNP* gene, which are characterized by prion protein amyloid deposits and abundant 3R+4R tau inclusions[44].

Also at a second level, the 4R tauopathies are divided into two classes. The PSP, GPT and GGT folds comprise three-layered core regions, in which R2 and R4 pack on either side of R3, whereas the packing of the C-terminal domain against part of R2 provides a fourth layer in the CBD and AGD folds. The division of 4R tauopathies on the basis of three-layered and four-layered folds agrees with observations on post-translational modifications, which showed similarities between PSP and GGT, and between CBD and cases with mutation +16 in intron 10 of *MAPT*[45]. A third level of classification for 4R tauopathies is provided by differences at the residue level between the three- and the four-layered folds.

The AGD fold is also found in ARTAG, consistent with the presence of granular or fuzzy astrocytes in grey matter in both conditions. AGD and ARTAG can develop with age and coexist in a given human brain with the Alzheimer tau fold. The AGD fold also makes up the tau filaments that are found in individuals with *MAPT* intron-10 mutations +3 and +16, consistent with the presence of argyrophilic grains in cases of the +3 mutation (Extended Data Fig. 7). Assembled tau in AGD has been reported to lack acetylation[46]. Features resembling AGD have also been described in cases of frontotemporal dementia caused by mutations S305I and S305S in exon 10 of *MAPT*[47,48]. These exonic mutations, and all known mutations in intron 10, destabilize the splicing regulatory element RNA of tau exon 10, which results in a relative overproduction of 4R tau and the formation of 4R tau filaments[49]. These filaments may have the AGD fold in common.

The structures that we present here are the first—to our knowledge— examples of structures of tau filaments from cases with *MAPT* mutations. They form following the relative overproduction of 4R tau. Other *MAPT* mutations cause the assembly of mutant tau, without overproduction[7]. Knowing the structures of tau filaments from cases in which mutations occur at residue P301[32,50–52] will be particularly important, as they have been used to produce the most widely used mouse models of human tauopathies[53,54]. It will be interesting to compare the tau folds from mouse and human brains.

It is notable how well neuropathologically confirmed diagnoses correlate with particular tau folds. For example, PSP and CBD have been grouped as clinically similar but neuropathologically distinct 4R tauopathies[55]. Their tau filament folds belong to different classes, confirming that they are separate disease entities. Before its definition, some cases of GGT were diagnosed as atypical PSP[56]. Our observations that the tau filaments from GGT-I and GGT-II are distinct from those of PSP support the definition of GGT as a separate neuropathological entity. Moreover, the observation that tau filaments from GGT-III do not twist suggests that GGT-III itself may be a different disease from GGT-I and GGT-II. Likewise, the observation that the structures of tau filaments from the second case of PSP-F are different from those of PSP and GGT suggests that this individual may have suffered from a distinct disease. Histologically, this case was also different from typical and atypical PSP. Because this case displayed abundant spherical, 4R tau-immunoreactive, basophilic neuronal inclusions in limbic and other brain regions, we name this disease 'limbic-predominant neuronal inclusion body 4R tauopathy' (LNT). Additional cases of LNT remain to be identified, and it is not yet clear whether other tau folds exist that are intermediate between those of PSP and GGT.

The molecular mechanisms that underlie tauopathies remain unknown. The presence of a specific tau fold in a given disease is consistent with its formation in a small number of brain cells, followed by the prion-like like spreading of tau inclusions[57]. This may underlie the temporospatial staging of disease[12,27]. Knowledge of the tau folds in the different diseases provides a framework for studying tauopathies that will lead to a better understanding of disease pathogenesis. At a diagnostic level, our findings will inform ongoing efforts to develop more specific and sensitive tau biomarkers.

Online content

Any methods, additional references, Nature Research reporting summaries, source data, extended data, supplementary information, acknowledgements, peer review information; details of author contributions and competing interests; and statements of data and code availability are available at https://doi.org/10.1038/s41586-021-03911-7.

1. Fitzpatrick, A. W. P. et al. Cryo-EM structures of tau filaments from Alzheimer's disease. *Nature* **547**, 185–190 (2017).
2. Falcon, B. et al. Tau filaments from multiple cases of sporadic and inherited Alzheimer's disease adopt a common fold. *Acta Neuropathol.* **126**, 699–708 (2013).
3. Falcon, B. et al. Structures of filaments from Pick's disease reveal a novel tau protein fold. *Nature* **561**, 137–140 (2018).
4. Falcon, B. et al. Novel tau filament fold in chronic traumatic encephalopathy encloses hydrophobic molecules. *Nature* **568**, 420–423 (2019).
5. Zhang, W. et al. Novel tau filament fold in corticobasal degeneration. *Nature* **580**, 283–287 (2020).
6. Goedert, M., Spillantini, M. G., Jakes, R., Rutherford, D. & Crowther, R. A. Multiple isoforms of human microtubule-associated protein tau: sequences and localization in neurofibrillary tangles of Alzheimer's disease. *Neuron* **3**, 519–526 (1989).
7. Ghetti, B. et al. Frontotemporal dementia caused by microtubule-associated protein tau gene (*MAPT*) mutations: a chameleon for neuropathology and neuroimaging. *Neuropathol. Appl. Neurobiol.* **41**, 24–46 (2015).
8. Shi, Y. et al. Cryo-EM structures of tau filaments from Alzheimer's disease with PET ligand APN-1607. *Acta Neuropathol.* **141**, 697–708 (2021).
9. Steele, J. C., Richardson, J. C. & Olszewski, J. Progressive supranuclear palsy. a heterogeneous degeneration involving the brainstem, basal ganglia and cerebellum with vertical gaze and pseudobulbar palsy, nuchal dystonia and dementia. *Arch. Neurol.* **10**, 333–359 (1964).
10. Williams, D. R. et al. Characteristics of two distinct clinical phenotypes in pathologically proven progressive supranuclear palsy: Richardson's syndrome and PSP-parkinsonism. *Brain* **128**, 1247–1258 (2005).
11. Höglinger, G. U. et al. Clinical diagnosis of progressive supranuclear palsy: the Movement Disorder Society criteria. *Mov. Disord.* **32**, 853–864 (2017).
12. Kovacs, G. G. et al. Distribution patterns of tau pathology in progressive supranuclear palsy. *Acta Neuropathol.* **140**, 99–119 (2020).
13. Sanders, D. W. et al. Distinct tau prion strains propagate in cells and mice and define different tauopathies. *Neuron* **82**, 1271–1288 (2014).
14. Molina, J. A. et al. Primary progressive aphasia with glial cytoplasmic inclusions. *Eur. Neurol.* **40**, 71–77 (1998).
15. Ahmed, Z. et al. Globular glial tauopathies (GGT) presenting with motor neuron disease or frontotemporal dementia: an emerging group of 4-repeat tauopathies. *Acta Neuropathol.* **122**, 415–428 (2011).
16. Ahmed, Z. et al. Globular glial tauopathies (GGT): consensus recommendations. *Acta Neuropathol.* **126**, 537–544 (2013).
17. Clark, C. N. et al. Temporal variant frontotemporal dementia is associated with globular glial tauopathy. *Cogn. Behav. Neurol.* **28**, 92–97 (2015).
18. Tanaka, H. et al. Globular glial tauopathy type II: clinicopathological study of two autopsy cases. *Neuropathology* **39**, 111–119 (2019).
19. Fu, Y. J. et al. Sporadic, four-repeat tauopathy with frontotemporal lobar degeneration, Parkinsonism, and motor neuron disease: a distinct clinicopathological and biochemical disease entity. *Acta Neuropathol.* **120**, 21–32 (2010).
20. Miki, Y., Mori, F., Hori, E., Kaimori, M. & Wakabayashi, K. Hippocampal sclerosis with four repeat tau-positive round inclusions in the dentate gyrus: a new type of four-repeat tauopathy. *Acta Neuropathol.* **117**, 713–718 (2009).
21. Kovacs, G. G. et al. Tauopathy with hippocampal 4-repeat tau immunoreactive spherical inclusions: a report of three cases. *Brain Pathol.* **28**, 274–283 (2018).
22. Borrego-Écija, S. et al. Tauopathy with hippocampal 4-repeat tau immunoreactive spherical inclusions in a patient with PSP. *Brain Pathol.* **28**, 284–286 (2018).
23. Nakane, T. et al. Single-particle cryo-EM at atomic resolution. *Nature* **587**, 152–156 (2020).
24. Braak, H. & Braak, E. Argyrophilic grains: characteristic pathology of cerebral cortex in cases of adult-onset dementia without Alzheimer changes. *Neurosci. Lett.* **76**, 124–127 (1987).
25. Braak, H. & Braak, E. Cortical and subcortical argyrophilic grains characterize a disease associated with adult-onset dementia. *Neuropathol. Appl. Neurobiol.* **15**, 13–26 (1989).
26. Tolnay, M. & Clavaguera, F. Argyrophilic grain disease: a late-onset dementia with distinctive features among tauopathies. *Neuropathology* **24**, 269–283 (2004).
27. Saito, Y. et al. Staging of argyrophilic grains: an age-associated tauopathy. *J. Neuropathol. Exp. Neurol.* **63**, 911–918 (2004).
28. Ferrer, I., Santpere, G. & Van Leeuwen, F. W. Argyrophilic grain disease. *Brain* **131**, 1416–1432 (2008).
29. Kovacs, G. G. et al. Aging-related tau astrogliopathy (ARTAG): harmonized evaluation strategy. *Acta Neuropathol.* **131**, 87–102 (2016).
30. Klotz, S. et al. Multiple system aging-related tau astrogliopathy with complex proteinopathy in an oligosymptomatic octogenarian. *Neuropathology* **41**, 72–83 (2021).
31. Spillantini, M. G. et al. Familial multiple system tauopathy with presenile dementia: a disease with abundant neuronal and glial tau filaments. *Proc. Natl Acad. Sci. USA* **94**, 4113–4118 (1997).
32. Hutton, M. et al. Association of missense and 5'-splice-site mutations in tau with the inherited dementia FTDP-17. *Nature* **393**, 702–705 (1998).
33. Spillantini, M. G. et al. Mutation in the tau gene in familial multiple system tauopathy with presenile dementia. *Proc. Natl Acad. Sci. USA* **95**, 7737–7741 (1998).
34. Forrest, S. L. et al. Retiring the term FTDP-17 as MAPT mutations are genetic forms of sporadic frontotemporal tauopathies. *Brain* **141**, 521–534 (2018).
35. Arai, T. et al. Identification of amino-terminally cleaved tau fragments that distinguish progressive supranuclear palsy from corticobasal degeneration. *Ann. Neurol.* **55**, 72–79 (2004).
36. Taniguchi-Watanabe, S. et al. Biochemical classification of tauopathies by immunoblot, protein sequence and mass spectrometric analyses of sarkosyl-insoluble and trypsin-resistant tau. *Acta Neuropathol.* **131**, 267–280 (2016).
37. Miki, T. et al. Factors associated with development and distribution of granular/fuzzy astrocytes in neurodegenerative diseases. *Brain Pathol.* **30**, 811–830 (2020).
38. Vidal, R. et al. A stop-codon mutation in the *BRI* gene associated with familial British dementia. *Nature* **399**, 776–781 (1999).
39. Vidal, R. et al. A decamer duplication in the 3' region of the *BRI* gene originates an amyloid peptide that is associated with dementia in a Danish kindred. *Proc. Natl Acad. Sci. USA* **97**, 4920–4925 (2000).
40. Holton, J. L. et al. Regional distribution of amyloid-Bri deposition and its association with neurofibrillary degeneration in familial British dementia. *Am. J. Pathol.* **158**, 515–526 (2001).
41. Holton, J. L. et al. Familial Danish dementia: a novel form of cerebral amyloidosis associated with deposition of both amyloid-Dan and amyloid-beta. *J. Neuropathol. Exp. Neurol.* **61**, 254–267 (2002).
42. Dan, A. et al. Extensive deamidation at asparagine residue 279 accounts for weak immunoreactivity of tau with RD4 antibody in Alzheimer's disease brain. *Acta Neuropathol. Commun.* **1**, 54 (2013).
43. Duyckaerts, C. et al. PART is part of Alzheimer disease. *Acta Neuropathol.* **129**, 749–756 (2015).
44. Hallinan, G. I. et al. Structure of tau filaments in prion protein amyloidoses. *Acta Neuropathol.* **142**, 227–241 (2021).
45. Kametani, F. et al. Comparison of common and disease-specific post-translational modifications of pathological tau associated with a wide range of tauopathies. *Front. Neurosci.* **14**, 581936.
46. Grinberg, L. T. et al. Argyrophilic grain disease differs from other tauopathies by lacking tau acetylation. *Acta Neuropathol.* **125**, 581–593 (2013).
47. Kovacs, G. G. et al. MAPT S305I mutation: implications for argyrophilic grain disease. *Acta Neuropathol.* **116**, 103–118 (2008).
48. Rönnbäck, A. et al. Neuropathological characterization of two siblings carrying the *MAPT* S305S mutation demonstrates features resembling argyrophilic grain disease. *Acta Neuropathol.* **127**, 297–298 (2014).
49. Varani, L. et al. Structure of tau exon 10 splicing regulatory element RNA and destabilization by mutations of frontotemporal dementia and parkinsonism linked to chromosome 17. *Proc. Natl Acad. Sci. USA* **96**, 8229–8234 (1999).
50. Poorkaj, P. et al. Tau is a candidate gene for chromosome 17 frontotemporal dementia. *Ann. Neurol.* **43**, 815–825 (1998).
51. Bugiani, O. et al. Frontotemporal dementia and corticobasal degeneration in a family with a P301S mutation in tau. *J. Neuropathol. Exp. Neurol.* **58**, 667–677 (1999).
52. Lladó, A. et al. A novel *MAPT* mutation (P301T) associated with familial frontotemporal dementia. *Eur. J. Neurol.* **14**, e9–e10 (2007).
53. Lewis, J. et al. Neurofibrillary tangles, amyotrophy and progressive motor disturbance in mice expressing mutant (P301L) tau protein. *Nat. Genet.* **25**, 402–405 (2000).
54. Allen, B. et al. Abundant tau filaments and nonapoptotic neurodegeneration in transgenic mice expressing human P301S tau protein. *J. Neurosci.* **22**, 9340–9351 (2002).
55. Coughlin, D. G., Dickson, D. W., Josephs, K. A. & Litvan, I. Progressive supranuclear palsy and corticobasal degeneration. *Adv. Exp. Med. Biol.* **1281**, 151–176 (2021).
56. Josephs, K. A. et al. Atypical progressive supranuclear palsy with corticospinal tract degeneration. *J. Neuropathol. Exp. Neurol.* **65**, 396–405 (2006).
57. Clavaguera, F. et al. Brain homogenates from human tauopathies induce tau inclusions in mouse brain. *Proc. Natl Acad. Sci. USA* **110**, 9535–9540 (2013).

Article

Methods

Data reporting

No statistical methods were used to predetermine sample size. The experiments were not randomized and the investigators were not blinded to allocation during experiments and outcome assessment.

Clinical history and neuropathology

We determined the cryo-EM structures of tau filaments from the brains of seven individuals with PSP, one individual with GGT-I, one individual with GGT-II, two individuals with AGD, one individual with ARTAG, two individuals with mutation +3 in intron 10 of *MAPT*, one individual with mutation +16 in intron 10 of *MAPT*, one individual with FBD and one individual with FDD. *MAPT* was sequenced in all cases. With the exception of the cases with +3 and +16 mutations, the sequences of *MAPT* exons and adjacent introns were wild type. As the *H2 MAPT* haplotype is of Caucasian origin[58] and many individuals were Japanese, we did not systematically determine *MAPT* haplotypes. PSP-RS case 1 was in an 83-year-old man who died with a neuropathologically confirmed diagnosis following a 4-year history of postural instability, supranuclear gaze palsy and cognitive impairment. Microscopic features showed degeneration of pallidum, tegmentum and dentate nucleus of the cerebellum. Abundant 4R tau-positive tangles, neuropil threads, tufted astrocytes and coiled bodies were in evidence. PSP-RS case 2 was in a 70-year-old man who died with a neuropathologically confirmed diagnosis following a 7-year history of postural instability, supranuclear gaze palsy and cognitive impairment. Magnetic resonance imaging (MRI) of the brain showed the hummingbird sign, probably reflecting a severe midbrain atrophy. PSP-RS case 3 was in a 74-year-old man who died following a 5-year history of postural instability, cognitive dysfunction and bulbar symptoms. Neuronal loss and gliosis, as well as abundant 4R tau-immunoreactive neuronal and glial tau inclusions, were present in the thalamus, subthalamic nucleus, cerebellum, midbrain, pons and medulla; 4R tau-immunoreactive argyrophilic grains were in evidence in the entorhinal cortex and hippocampus. The neuropathological diagnosis was PSP and AGD. PSP-F case 1 was in a 62-year-old man who died with a neuropathologically confirmed diagnosis following an 11-year history of behavioural-variant FTD, postural instability and bulbar symptoms. Abundant neuronal and glial 4R tau inclusions were present in cortical and, especially, subcortical areas. Basal ganglia, thalamus and brainstem were severely affected. PSP-F case 2 was in a 66-year-old woman who died with FTD and parkinsonism. Abundant neuronal and glial 4R tau inclusions were present in cortical and subcortical areas. In limbic areas and other brain regions, abundant spherical, 4R tau-immunoreactive, basophilic and Gallyas silver-positive neuronal inclusions were present, together with globular glial tau inclusions. The case of PSP-P was in a 63-year-old man who died with a neuropathologically confirmed diagnosis following a 9-year history of akinetic-rigid parkinsonism, postural instability and cognitive impairment. Brain MRI showed progressive frontal atrophy and mild midbrain atrophy. Neuronal loss was more marked in the substantia nigra than in the pallidum, tegmentum and dentate nucleus of the cerebellum. Abundant neuronal and glial 4R tau pathology was widespread. The case of PSP-CBS was in an 88-year-old woman with a neuropathologically confirmed diagnosis following a 9-year history of corticobasal syndrome, cerebellar ataxia and cognitive impairment. Abundant neuronal and glial 4R tau inclusions were present in the cerebral cortex, from the precentral gyrus to the operculum. The case of GGT-I was in a 77-year-old woman with a neuropathologically confirmed diagnosis following a 3-year history of falls, bradykinesia and cognitive impairment. The clinical diagnosis was behavioural-variant FTD with an atypical parkinsonian disorder[17]. Neuropathologically, severe anterior frontal and temporal cortical nerve cell loss and severe tau deposition in cerebral cortex and subcortical white matter were in evidence. Abundant neuronal, as well as globular oligodendroglial and astrocytic

4R tau inclusions, were present. The case of GGT-II was in a 76-year-old woman with a neuropathologically confirmed diagnosis following a 5-year history of asymmetric pyramidal signs, diffuse muscle atrophy and dysarthria[18]. Severe neuronal loss was present in the motor cortex, with an almost complete loss of Betz cells. Abundant 4R tau neuronal cytoplasmic inclusions, globular oligodendroglial inclusions, coiled bodies and neuropil threads were in evidence. Only a small number of globular astroglial inclusions was seen in the affected cerebral cortex. The case of GGT-III was in a 62-year-old man with a neuropathologically confirmed diagnosis following a 4-year history of parkinsonism, motor signs and dementia[19]. Loss of anterior horn cells and degeneration of the corticospinal tract were in evidence. Abundant 4R tau neuronal and globular oligodendroglial and astroglial inclusions were present. Tau filament structures were determined from the nucleus accumbens of two cases of AGD with a predominantly neuronal 4R tau pathology. The first case was in a 90-year-old man with a 6-year history of memory loss and behavioural changes. By imaging, diffuse atrophy of the medial temporal lobe was observed. At autopsy, a chronic subdural haematoma was present on the right side, supporting the possibility of a previous head injury and consistent with the presence of CTE type I tau filaments. However, there was no history of head trauma. Nerve cell loss and numerous tau-immunoreactive argyrophilic grains were observed in the entorhinal cortex, hippocampus and amygdala. Some tau-immunoreactive coiled bodies and bush-like astrocytes were also present. The second case of AGD was in an 85-year-old man with a 3-year history of postural instability and memory loss. At autopsy, atrophy of the hippocampus, amygdaloid nucleus and parahippocampal gyrus was present. Abundant 4R tau-immunoreactive argyrophilic grains were in evidence, with some coiled bodies and bush-like astrocytes. ARTAG was identified in an 85-year-old woman with a one-year history of cancer and depression[30]. At autopsy, she had prominent ARTAG (subpial, subependymal, grey matter, white matter and perivascular). A heterozygous mutation at position +3 in intron 10 of *MAPT* was identified in two patients with dementia and a family history of multiple system tauopathy with presenile dementia (MSTD). The first individual was a 54-year-old woman who died following a 7-year history of disinhibition, anxiety and cognitive impairment. The second individual with a +3 mutation in intron 10 of *MAPT* was a 63-year-old woman who died following an 8-year history of dementia with a severe amnestic component. In both individuals, nerve cell loss and gliosis were severe in the neocortex, amygdala, entorhinal cortex, hippocampus, basal ganglia, subthalamic nucleus, midbrain and brainstem. Widespread silver-positive neuronal, oligodendroglial and astrocytic 4R tau inclusions were in evidence. A mutation at position +16 in intron 10 of *MAPT* was identified in a 53-year-old man with a 7-year history of behavioural-variant FTD. This individual had a family history of FTD, consistent with dominant inheritance. Abundant 4R tau neuronal and glial cell inclusions were in evidence. Some glial cell inclusions resembled astrocytic plaques. The case of FBD (T to A mutation, removing the stop codon in *ITM2B*) was in a 68-year-old woman with an 11-year history of ataxia and progressive cognitive decline. Her speech became slurred and she experienced problems with swallowing. A brother and two uncles had similar symptoms. As reported previously (case 5 in ref. [40]), neuropathological findings included degeneration of the hemispheric white matter and parenchymal and blood vessel deposits of British amyloid, as well as widespread neurofibrillary pathology. This patient had a serious bicycle accident, probably as a result of ataxia, which may explain the presence of CTE type I filaments. The case of FDD (decamer duplication between codons 265 and 266 of *ITM2B*) was in a 52-year-old man from generation V of a previously described kindred[41]. He developed cataracts aged 21 and had severe hearing loss, nystagmus and ataxia aged 38. Neuropathological examination showed similar findings as in FBD, with the difference that Danish amyloid, which differs from British amyloid in its 12 C-terminal amino acids, formed mostly thioflavin S-negative deposits.

Whole-exome sequencing

Target enrichment made use of the SureSelectTX human all-exon library (V6, 58 mega base pairs; Agilent) and high-throughput sequencing was carried out using a HiSeq4,000 (2 × 75-base-pair paired-end configuration; Illumina). Bioinformatics analyses were performed as described[59]

Extraction of tau filaments

For cryo-EM, sarkosyl-insoluble material was extracted from frontal cortex (PSP-RS case 1, PSP-RS case 2, PSP-P, PSP-CBS, GGT-I, GGT-II, GGT-III, +3 case 1, +3 case 2, +16), temporal cortex (PSP-F case 2, FDD), entorhinal cortex (PSP-RS case 3), hippocampus (FBD, ARTAG), putamen (PSP-F case 1), thalamus (PSP-RS case 3) and nucleus accumbens (AGD cases 1 and 2), essentially as described[36]. In brief, tissues were homogenized in 20 volumes (v/w) extraction buffer consisting of 10 mM Tris-HCl, pH 7.5, 0.8 M NaCl, 10% sucrose and 1 mM EGTA. Homogenates were brought to 2% sarkosyl and incubated for 30 min at 37 °C. Subsequent steps were performed at 4 °C. For PSP-RS case 1, PSP-RS case 2, PSP-CBS, PSP-P, GGT-II, GGT-III, AGD case 1, AGD case 2, +3 case 1, +3 case 2 and the +16 case, after a 10-min centrifugation at 20,000g, the supernatants were spun at 100,000g for 20 min. For the rest of the cases, the supernatants from a 10-min centrifugation at 7,000g were spun at 100,000g for 60 min. The pellets were resuspended in 700 µl g^{-1} extraction buffer and centrifuged at 9,500g for 10 min. For PSP-RS case 1, PSP-RS case 2, PSP-CBS, PSP-P, GGT-II, GGT-III, AGD case 1, AGD case 2 and the +16 case, the supernatants were diluted threefold in 50 mM Tris-HCl, pH 7.5, containing 0.15 M NaCl, 10% sucrose and 0.2% sarkosyl, and spun at 166,000g for 30 min. For the other cases, the supernatants were spun at 100,000g for 60 min, and the pellets were resuspended in 700 µl g^{-1} extraction buffer and centrifuged at 9,800g. The supernatants were then spun at 100,000g for 60 min. Sarkosyl-insoluble pellets were resuspended in 25 µl g^{-1} of 20 mM Tris-HCl, pH 7.4 and 100 mM NaCl and used for cryo-EM. It was previously shown that sarkosyl does not influence the Alzheimer tau fold[8].

Immunoblotting, histology and silver staining

Immunoblotting was carried out as described[36]. Samples were resolved using 4–20% Tris-glycine gels (Novex) and antibody T46 was used at 1:2,000. Histology and immunohistochemistry were carried out as described[60]. Brain sections were 8 µm thick and were counterstained with haematoxylin. Primary antibodies were: RD3 (1:1,000); RD4 (1:1,000); AT8 (1:300). Sections were silver-impregnated using the method of Gallyas-Braak[61].

Cryo-EM

Extracted tau filaments were centrifuged at 3,000g for 60 s, before being applied to glow-discharged holey carbon grids (Quantifoil Au R1.2/1.3, 300 mesh) and plunge-frozen in liquid ethane using a Thermo Fisher Vitrobot Mark IV. Images for PSP-F case 2 were acquired on a 300 keV Thermo Fisher Titan Krios G4 microscope, described previously[23], which was equipped with a cold field-emission gun, a Selectrix X energy filter and a Falcon-IV detector. The energy filter was operated with a slit width of 10 eV. Images were recorded at a total dose of 50 e$^-$ Å^{-2} using aberration-free image shift (AFIS) as incorporated within the Thermo Fisher EPU software at a throughput of 300 images per hour in EER format[62]. All other datasets were acquired using EPU software on Thermo Fisher Titan Krios microscopes with either a Gatan K2 or K3 detector, using a GIF-quantum energy filter (Gatan) with a slit width of 20 eV to remove inelastically scattered electrons. All datasets were collected in counting mode, except for the +3 case 1 and the GGT-III case, which were collected in super-resolution mode. Further details are given in Extended Data Table 1.

Helical reconstruction

Movie frames were gain-corrected, aligned, dose-weighted and then summed into a single micrograph using RELION's own motion correction program[63]. The micrographs were used to estimate the contrast transfer function (CTF) using CTFFIND4.1[64]. All subsequent image-processing steps were performed using helical reconstruction methods in RELION[65,66]. The filaments from PSP-F case 2, FBD and FDD were picked by crYOLO;[67] the rest of the filaments were selected manually in the micrographs. For the +3 and +16 cases, filaments of different types were picked separately; for the other datasets different filament types were separated on the basis of the appearance of 2D class averages. For all datasets, reference-free 2D classification was performed to select suitable segments for further processing. Initial 3D reference models were generated de novo from the 2D class averages using an estimated rise of 4.75 Å and helical twists according to the observed crossover distances of the filaments in the micrographs[68] for all datasets, except those from the thalamus of PSP-RS case 3, PSP-P, PSP-F case 1, GGT-II, AGD case 2 and ARTAG. Combinations of 3D auto-refinements and 3D classifications were then used to select the best segments for each structure. For all datasets, Bayesian polishing and CTF refinement[69] were performed to further increase the resolution of the reconstructions. For PSP-F case 2, temporal drift in the beam tilt was corrected by grouping every 8,000 consecutively collected segments into separate optics groups before CTF refinement. Final reconstructions were sharpened using the standard post-processing procedures in RELION, and overall final resolutions were estimated from Fourier shell correlations at 0.143 between the two independently refined half-maps, using phase-randomization to correct for convolution effects of a generous, soft-edged solvent mask[70]. Further details of data acquisition and processing are provided in Extended Data Table 1, Supplementary Tables 1–3.

Model building and refinement

Where multiple structures from different cases were obtained, atomic models were only built and refined in the best available maps. For the PSP structure, this was PSP-RS case 1; for the GGT structures, this was GGT-I; for the GPT structures this was PSP-F case 2; for the AGD type 1 filament, this was AGD case 1; for the AGD type 2 filament, this was +16. Atomic models were built manually using Coot[71]. Side-chain clashes were detected using MolProbity[72] and corrected by iterative cycles of real-space refinement in Coot and Fourier-space refinement in REFMAC[73] and/or real-space refinement in PHENIX[74]. For each refined structure, separate model refinements were performed against a single half-map, and the resulting model was compared to the other half-map to confirm the absence of overfitting (Extended Data Fig. 3). Figures were prepared using ChimeraX[75] and PyMOL (Schrödinger). Statistics for the final models are shown in Extended Data Table 1.

Ethical review processes and informed consent

The studies that were performed at Tokyo Metropolitan Institute of Medical Science, Indiana University, UCL Queen Square Institute of Neurology, Medical University of Vienna and the University of Toronto were approved by the ethics committees and through the ethical review processes at each institution. Informed consent was obtained from the patients' next of kin.

Reporting summary

Further information on research design is available in the Nature Research Reporting Summary linked to this paper.

Data availability

Cryo-EM maps have been deposited in the Electron Microscopy Data Bank (EMDB) under accession numbers EMD-13218 for PSP, EMD-13219

Article

for GGT-I, EMD-13220 for GGT-II, EMD-13221 for GGT-III, EMD-13223 for GPT type 1a, EMD-13224 for GPT type 1b, EMD-13225 for GPT type 2, EMD-13226 for AGD type 1 and EMD-13227 for AGD type 2. Corresponding refined atomic models have been deposited in the Protein Data Bank (PDB) under accession numbers 7P65 for PSP, 7P66 for GGT type 1, 7P67 for GGT type 2, 7P68 for GGT type 3, 7P6A for GPT type 1a, 7P6B for GPT type 1b, 7P6C for GPT type 2, 7P6D for AGD type 1 and 7P6E for AGD type 2. Cryo-EM datasets have been deposited in the Electron Microscopy Public Image Archive (EMPIAR) under accession numbers 10765 for PSP-RS case 1, 10766 for the GGT-I case, 10767 for PSP-F case 2, 10768 for AGD case 1, and 10769 for the +16 case. Any other relevant data are available from the corresponding authors upon request.

58. Evans, W. et al. The tau *H2* haplotype is almost exclusively Caucasian in origin. *Neurosci. Lett.* **369**, 183–185 (2004).
59. Farlow, J. L. et al. Whole-exome sequencing in familial Parkinson's disease. *JAMA Neurol.* **73**, 68–75 (2016).
60. Spina, S. et al. The tauopathy associated with mutation +3 in intron 10 of *Tau*: characterization of the MSTD family. *Brain* **131**, 72–89 (2008).
61. Braak, H., Braak, E., Ohm, T. & Bohl, J. Silver impregnation of Alzheimer's neurofibrillary changes counterstained for basophilic material and lipofuscin pigment. *Stain Technol.* **69**, 197–200 (1988).
62. Guo, H. et al. Electron-event representation data enable efficient cryoEM file storage with full preservation of spatial and temporal resolution. *IUCrJ* **7**, 860–869 (2020).
63. Zivanov, J. et al. A Bayesian approach to beam-induced motion correction in cryo-EM single-particle analysis. *IUCrJ* **6**, 5–17 (2020).
64. Rohou, A. & Grigorieff, N. CTFFIND4: fast and accurate defocus estimation from electron micrographs. *J. Struct. Biol.* **192**, 216–221.
65. He, S. & Scheres, S. H. W. Helical reconstruction in RELION. *J. Struct. Biol.* **198**, 163–176 (2017).
66. Zivanov, J. et al. New tools for automated high-resolution cryo-EM structure determination in RELION-3. *Elife* **7**, e42166 (2018).
67. Wagner, T. et al. SPHIRE-crYOLO is a fast and accurate fully automated particle picker for cryo-EM. *Commun. Biol.* **2**, 218 (2019).
68. Scheres, S. H. W. Amyloid structure determination in RELION-3.1. *Acta Crystallogr. D* **76**, 94–101 (2020).
69. Zivanov, J. et al. Estimation of high-order aberrations and anisotropic magnification from cryo-EM data sets in RELION-3.1. *IUCrJ* **7**, 253–267 (2020).
70. Chen, S. et al. High-resolution noise substitution to measure overfitting and validate resolution in 3D structure determination by single particle electron cryomicroscopy. *Ultramicroscopy* **135**, 24–35 (2013).
71. Casañal, A. et al. Current developments in Coot for macromolecular model building of electron cryo-microscopy and crystallographic data. *Protein Sci.* **29**, 1069–1078 (2020).
72. Williams, C. J. et al. MolProbity: more and better reference data for improved all-atom structure validation. *Protein Sci.* **27**, 293–315 (2018).
73. Brown, A. et al. Tools for macromolecular model building and refinement into electron cryo-microscopy reconstructions. *Acta Crystallogr. D* **71**, 136–153 (2015).
74. Afonine, P. V. et al. Real-space refinement in PHENIX for cryo-EM and crystallography. *Acta Crystallogr. D* **74**, 531–544 (2018).
75. Pettersen, E. F. et al. UCSF ChimeraX: structure visualization for researchers, educators, and developers. *Protein Sci.* **30**, 70–82 (2021).

PSP-RS case 1 · **PSP-RS case 2** · **PSP-RS case 3 (Tha)** · **PSP-CBS** · **PSP-P** · **PSP-F case 1** · **PSP-F case 2** · **GGT-I** · **GGT-II** · **GGT-III** · **+16** · **+3 case 1** · **+3 case 2** · **AGD case 1** · **AGD case 2** · **PSP-RS case 3 (EC)** · **ARTAG** · **FBD** · **FDD**

Extended Data Fig. 1 | Tau immunohistochemistry. Representative tau staining of the brain regions used for cryo-EM structure determination (see Methods), using antibody AT8 (pS202/pT205 tau). Scale bars are 50 µm, except for GGT Type I, FBD and FDD, for which they are 25 µm. For PSP-RS case 3, both the thalamus (Tha) and the entorhinal cortex (EC) are shown. Similar results were obtained using a minimum of six additional stained sections for each case.
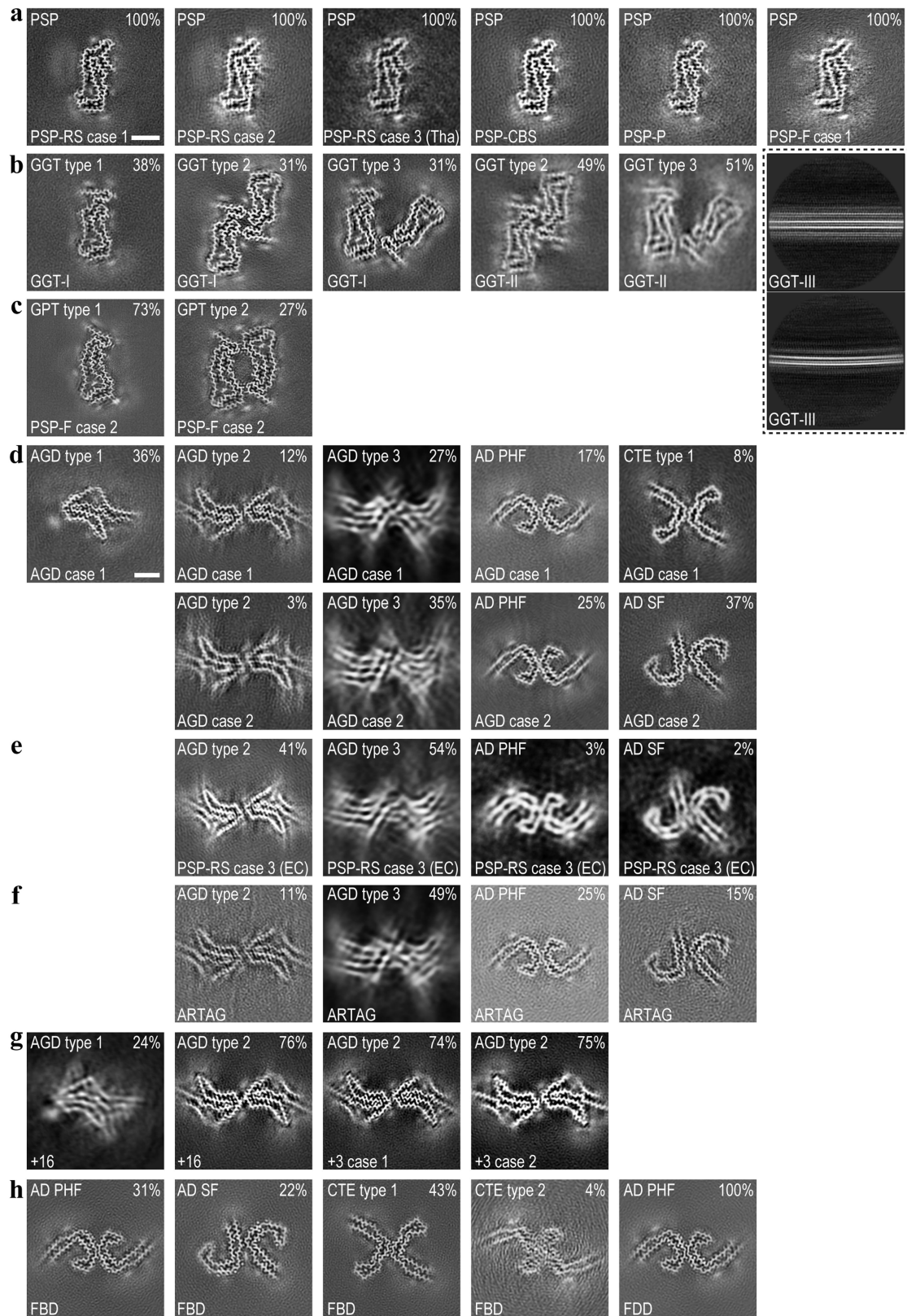
Extended Data Fig. 2 | Cryo-EM reconstructions. a, Cryo-EM maps for tau filaments from six cases of PSP. For each map, a sum of the reconstructed density for several XY-slices is shown, corresponding to approximately 4.7 Å. The disease cases are referenced at the bottom of each image, the filament types at the top left and the percentages of a given filament type among the tau filaments in the dataset at the top right. Scale bar 5 nm. The same scale applies to all panels, except **d–g**. **b–h**, As in **a**, but a case of GGT-I and a case of GGT-II (**b**); a case diagnosed as PSP-F, but that contains filaments with the PGT fold (**c**); two cases of AGD (**d**); scale bar 5nm, the same scale applies to panels **d–g**; entorhinal cortex of PSP-RS case 3 (**e**); a case of ARTAG (**f**); three cases with mutations +16 or +3 in intron 10 of *MAPT* (**g**); a case of FBD and a case of FDD (**h**). Panels **d–f** contain blank squares to indicate the absence of AGD type I filaments in some cases. The inset with dashed lines shows 2D class average images of tau filaments from a case of GGT-III without apparent twist.
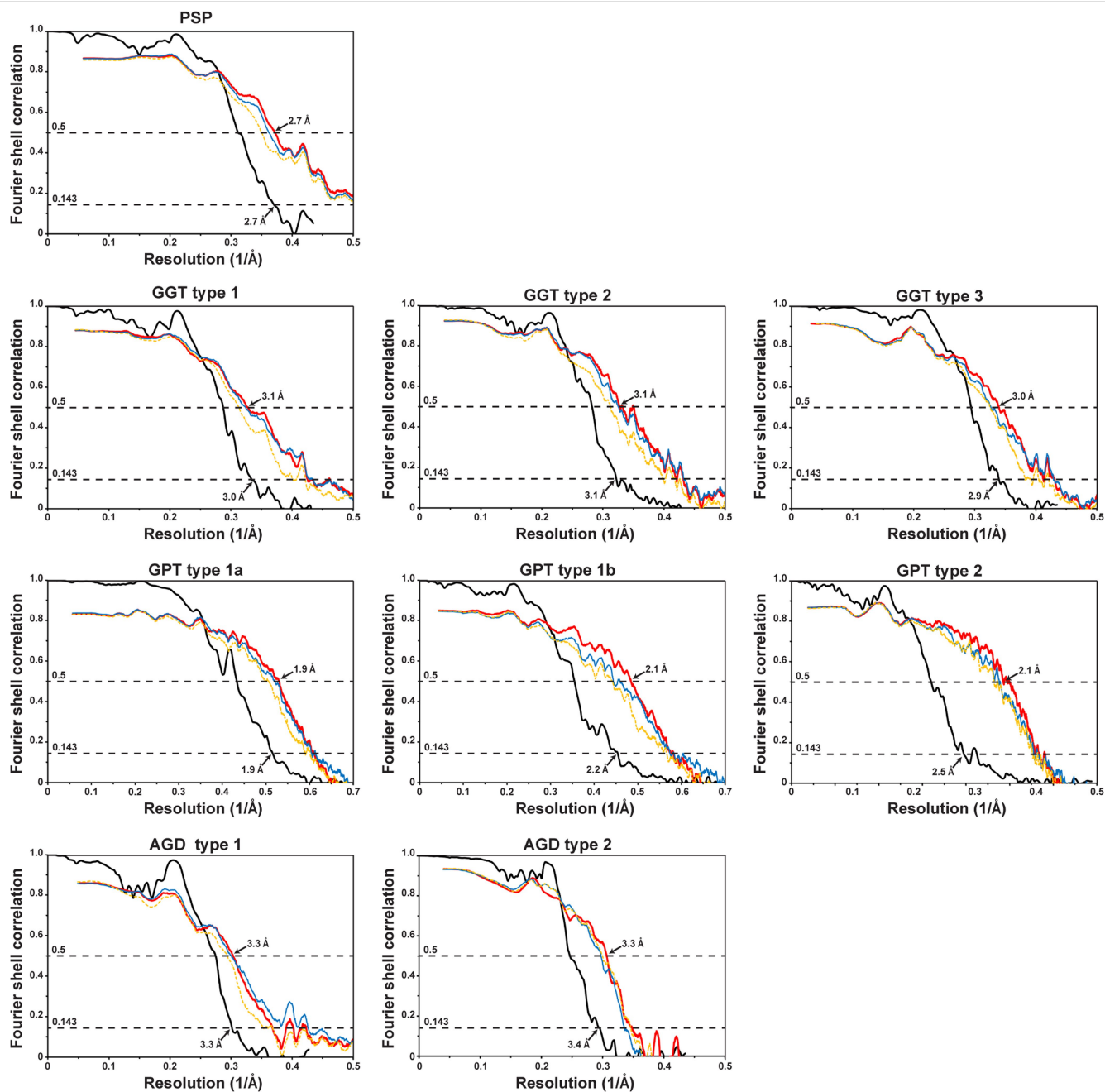
Extended Data Fig. 3 | Cryo-EM resolution estimates. Fourier Shell Correlation (FSC) curves for cryo-EM maps and atomic structures of PSP filaments (from PSP-RS case 1); GGT filament types 1-3 (from GGT-I); GPT filament types 1a, 1b and 2 (from PSP-F case 2); and AGD filament types 1 and 2 (from AGD case 1 and the +16 case, repectively). FSC curves are shown for two independently refined cryo-EM half-maps (black); for the final refined atomic model against the final cryo-EM map (red); for the atomic model refined in the first half-map against that half-map (blue); and for the refined atomic model in the first half-map against the other half-map (yellow).
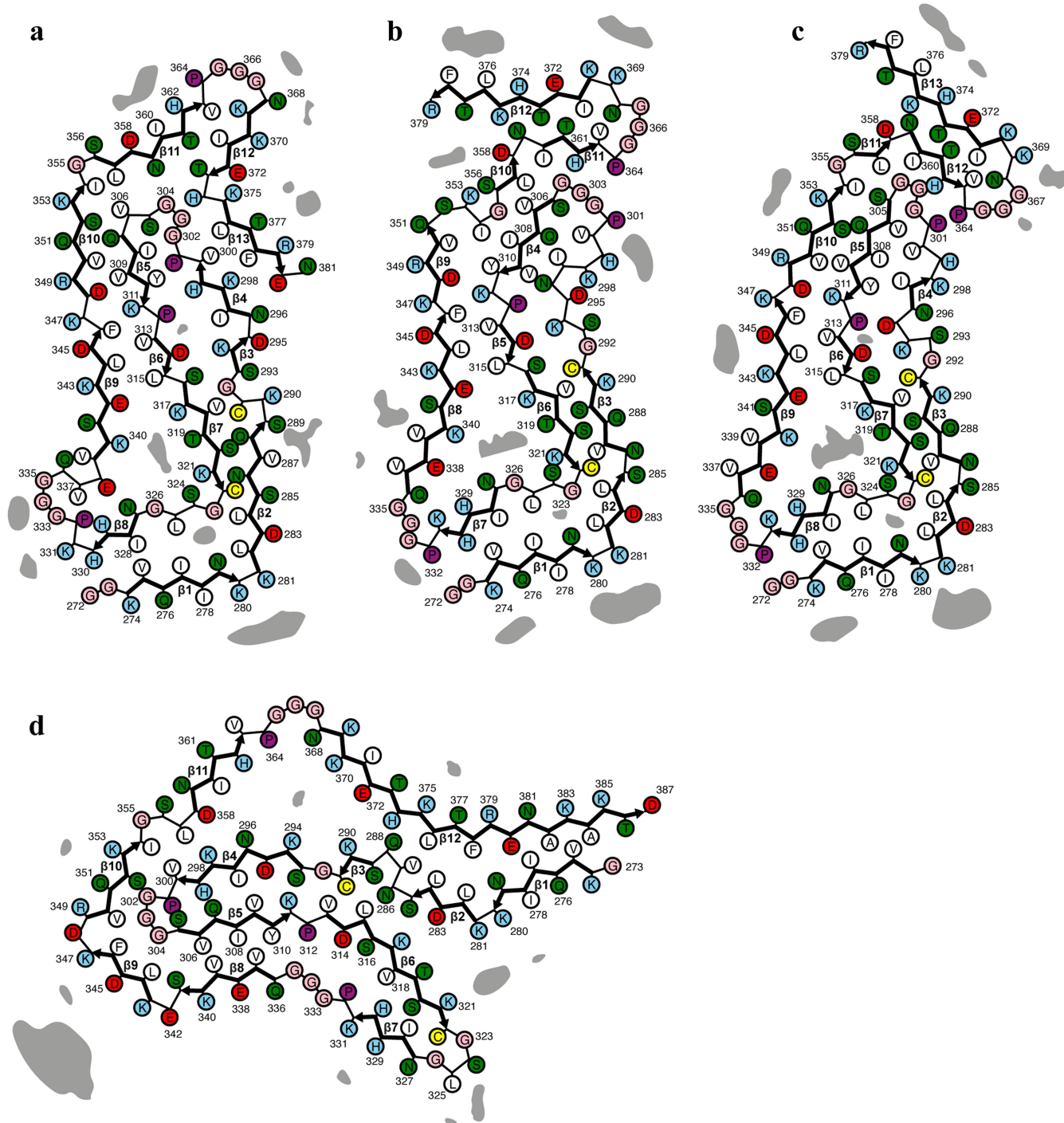
Extended Data Fig. 4 | Schematics of tau filament folds. a–d, Schematics of the tau folds for PSP (**a**), GGT (**b**), GPT (**c**) and AGD (**d**). Negatively charged residues are shown in red, positively charged residues in blue, polar residues in green, apolar residues in white, sulfur-containing residues in yellow, prolines in purple and glycines in pink. Thick connecting lines with arrow heads are used to indicate β-strands; additional densities are shown in grey.
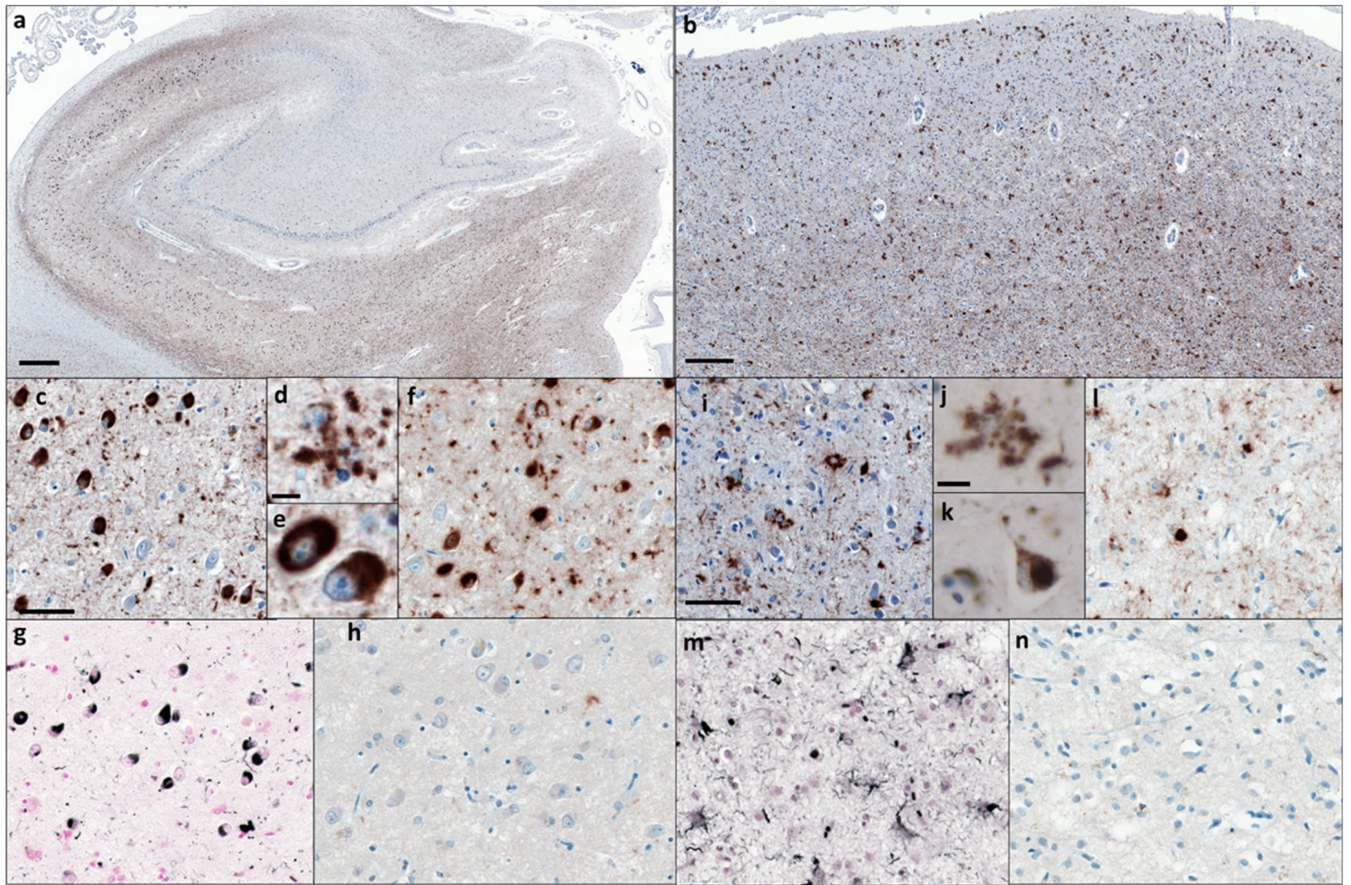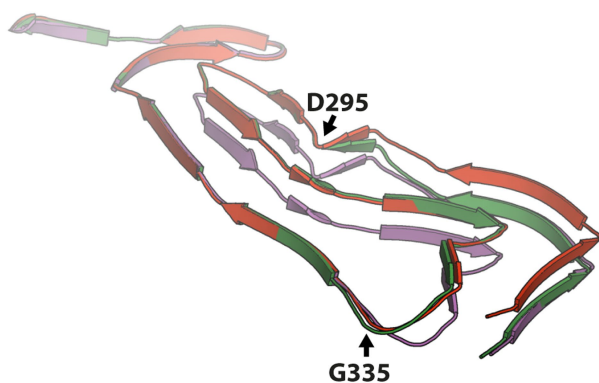
Extended Data Fig. 5 | Tau pathology in limbic-predominant neuronal inclusion body 4R tauopathy (LNT, PSP-F case 2). a, Low power view of hippocampus stained with antibody AT8 (pS202/pT205tau). **b**, Low power view of frontal cortex stained with AT8. **c**, Higher power view of hippocampus stained with AT8. **d**, AT8-positive globular astrocyte in hippocampus. **e**, AT8-positive neurons in hippocampus. **f**, Hippocampus stained with antibody RD4 (specific for 4R tau). **g**, Gallyas-Braak silver-positive neurons and glial cells in hippocampus. **h**, Hippocampus stained with antibody RD3 (specific for 3R tau). **i**, Higher-power view of frontal cortex stained with AT8. **j**, AT8-positive globular astrocyte in frontal cortex. **k**, AT8-positive neurons in frontal cortex. **l**, Frontal cortex stained with RD4. **m**, Gallyas-Braak silver-positive neurons and glial cells in frontal cortex. **n**, Frontal cortex stained with RD3. Representative images are shown. Similar results were obtained using a minimum of six additional stained sections for each panel. Scale bars: 400 µm in (**a**); 200 µm in (**b**), 50 µm in (**c**, **f**, **g**, **h**, **i**, **l**, **m**, **n**); 10 µm in (**d**, **e**, **j**, **k**).

a

D295

G335

GPT type 1a   **GPT type 1b**   **GPT type 2**

b

PSP   **GGT**   **GPT**

c

N286
S285
K369
D283
K370
K281

GGT type 3   **GPT type 2**

d

L357
S293
E380
N381
D387
K274
G273
K274
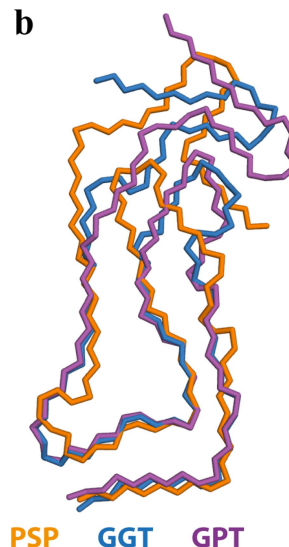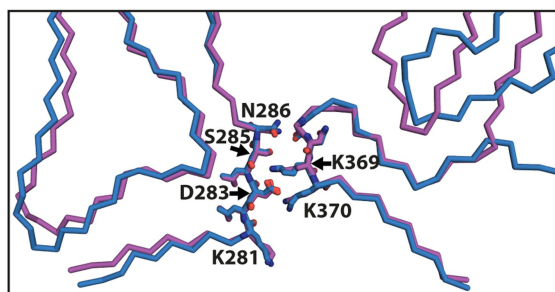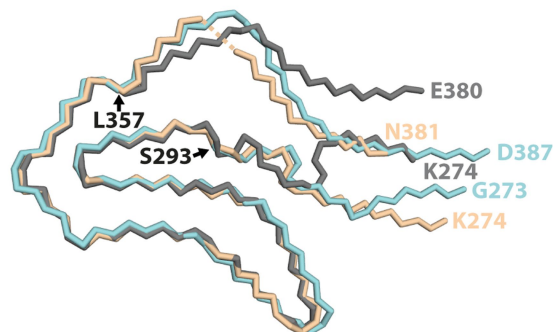
AGD type 1   **AGD type 2**   **CBD**

Extended Data Fig. 6 | Structural comparisons. a, Comparison of two different main-chain conformations for GPT type 1 filaments (type 1a in purple; type 1b in green) and the main-chain conformation of GPT type 2 filaments (red). **b**, Comparison of the PSP (orange), GGT (blue) and GPT (purple) folds. **c**, Comparison of the inter-protofilament interfaces of GGT type 3 and GPT type 2 filaments. **d**, Comparison of the AGD type 1 (light blue), AGD type 2 (pink) and CBD (grey) folds.
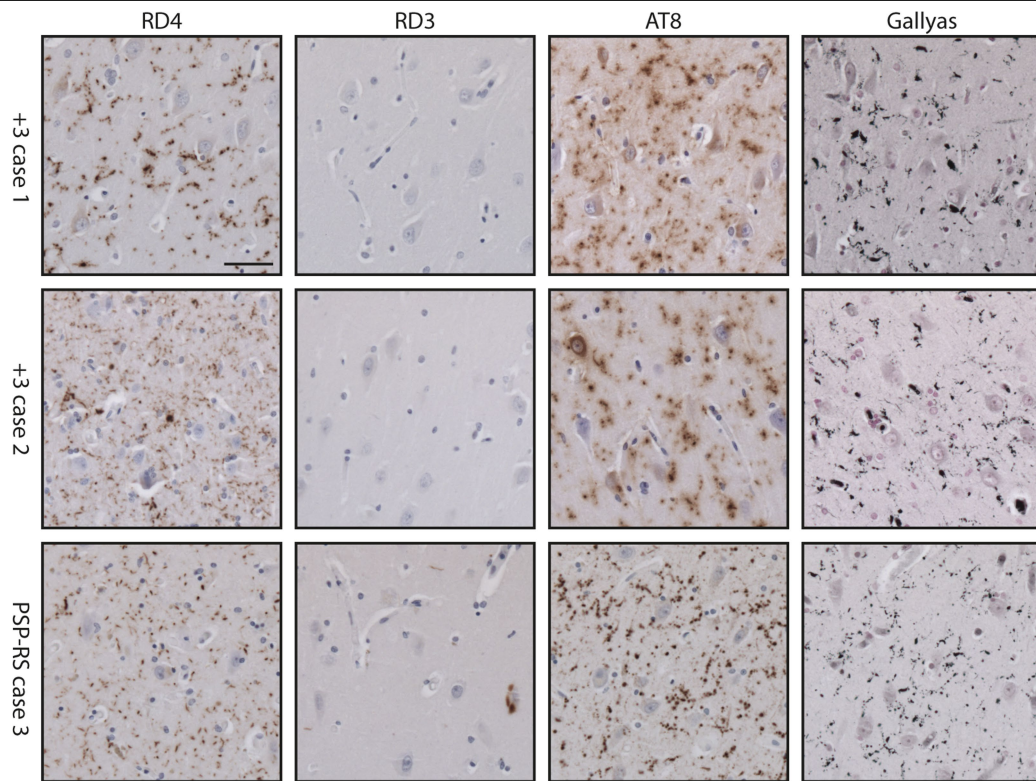
Extended Data Fig. 7 | Argyrophilic grains in the entorhinal cortex. Representative tau staining with antibodies RD4 (4R tau), RD3 (3R tau), AT8 (pS202/pT205 tau), as well as Gallyas-Braak silver, of the entorhinal cortex from cases 1 and 2 with mutation +3 in intron 10 of *MAPT* and from case 3 of PSP-RS. Similar results were obtained using a minimum of six additional stained sections for each case. Scale bar, 50 μm.

Article
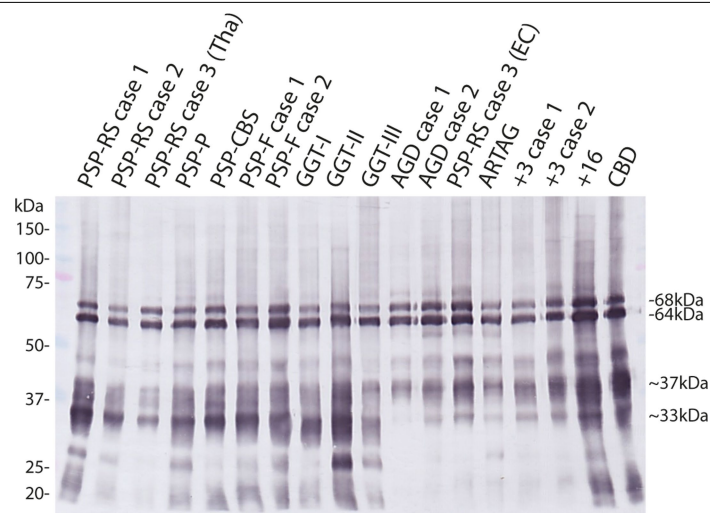
Extended Data Fig. 8 | Immunoblot analysis of 4R tauopathies.
Hyperphosphorylated full-length tau (64 and 68 kDa) and C-terminal fragments (33 kDa and 37 kDa) were detected in sarkosyl-insoluble fractions from the brain regions used for cryo-EM by anti-tau antibody T46. A prominent 33-kDa band was characteristic of PSP and GGT; strong 37-kDa bands were in evidence in AGD, ARTAG, cases with intron 10 mutations in *MAPT* (+3 and +16) and in CBD. PSP-RS case 3 had a strong 33-kDa band in thalamus (Tha) and strong 37-kDa bands in entorhinal cortex (EC), consistent with AGD co-pathology. Similar results were obtained in three independent experiments. The original, uncropped image is available in Supplementary Fig. 1.

Extended Data Table 1 | Cryo-EM data collection, refinement and validation statistics

	PSP-RS case 1	GGT-I case 1	PSP-F case 2	+16 case 1
Data collection and processing				
Electron Gun	XFEG	XFEG	CFEG	XFEG
Detector	K2	K2	Falcon4	K2
Energy filter slit width (eV)	20	20	10	20
Voltage (kV)	300	300	300	300
Electron exposure (e−/Å²)	40	50	50	54
Defocus range (μm)	1.7-2.2	1.5-2.5	0.8-2.0	1.7-2.8
Physical pixel size (Å)	1.15	1.15	0.727	1.15
Initial particle images (no.)	155,030	408,018	630,640	375,898

	PSP-RS case 1	GGT-I case 1 type 1	GGT-I case 1 type 2	GGT-I case 1 type 3	PSP-F case 2 type 1a	PSP-F case 2 type 1b	PSP-F case 2 type 2	+16 case 1 type 1	+16 case 1 type 2
Symmetry imposed	C1	C1	C1	C1	C1	C1	C1	C1	C2
Final particle images (no.)	17,316	14,873	42,381	84,438	53,363	15,096	16,813	14,582	52,134
Map resolution (Å; FSC=0.143)	2.7	3.0	3.1	2.9	1.9	2.2	2.5	5.7	3.4
Helical rise (Å)	4.78	4.78	2.37	4.75	4.78	4.78	2.39	4.80	4.80
Helical twist (°)	-0.86	-0.75	179.65	-0.73	-0.36	-0.39	179.82	-0.36	-0.40

	PSP-RS case 1 type 1	GGT-I case 1 type 1	GGT-I case 1 type 2	GGT-I case 1 type 3	PSP-F case 2 type 1a	PSP-F case 2 type 1b	PSP-F case 2 type 2	AGD case 1 type 1	+16 case 1 type 2
Refinement									
Initial model used (PDB code)	-	-	-	-	-	-	-	6TJX	6TJX
Model resolution (Å) FSC threshold	2.7	3.1	3.1	3.0	1.9	2.1	2.1	3.3	3.3
Map sharpening B factor (Å²)	-12.35	-18.84	-34.53	-29.03	-18.17	-20.13	-23.15	-37.67	-35.83
Model composition									
Non-hydrogen atoms	4145	4060	8120	8120	4166	4060	8120	4340	4854
Protein residues	550	540	1080	1080	540	540	1080	575	630
Waters	-	-	-	-	76	-	-	-	-
B factors (Å²)									
Protein	20.48	59.98	31.47	32.64	35.65	33.87	51.25	2.98	107.39
Waters	-	-	-	-	30.00	-	-	-	-
R.m.s. deviations									
Bond lengths (Å)	0.004	0.004	0.007	0.006	0.004	0.004	0.005	0.003	0.009
Bond angles (°)	0.627	0.661	1.057	0.903	0.718	0.748	0.803	0.655	1.298
Validation									
MolProbity score	1.11	1.46	1.48	1.43	1.38	1.46	1.22	1.13	1.65
Clashscore	2.01	4.21	3.61	4.45	3.33	4.21	2.77	2.25	4.83
Poor rotamers (%)	0.00	0.00	0.00	0.00	0.00	0.00	0.00	0.00	0.00
Ramachandran plot									
Favored (%)	97.22	96.23	95.28	96.70	96.23	96.23	97.17	97.35	94.06
Allowed (%)	2.78	3.77	4.72	3.30	3.77	3.77	2.83	2.65	5.94
Disallowed (%)	0.00	0.00	0.00	0.00	0.00	0.00	0.00	0.00	0.00
PDB	7P65	7P66	7P67	7P68	7P6A	7P6B	7P6C	7P6D	7P6E
EMDB	13218	13219	13220	13221	13223	13224	13225	13226	13227
EMPIAR	10765	10766			10767			10768	10769

Extended Data Table 2 | Cases of tauopathy used for cryo-EM

Tauopathy	Case number	Gender	Age at death (y)	Brain regions
PSP Richardson's syndrome (PSP-RS)	1	M	83	Frontal cortex
	2	M	70	Frontal cortex
	3	M	74	Thalamus; Entorhinal cortex
PSP with a predominant frontal presentation (PSP-F)	1	M	62	Putamen
	2	F	66	Temporal cortex
PSP with predominant parkinsonism (PSP-P)	1	M	63	Frontal cortex
PSP with a predominant presentation of corticobasal syndrome (PSP-CBS)	1	F	88	Frontal cortex
GGT Type I	1	F	77	Frontal cortex
GGT Type II	1	F	76	Frontal cortex
GGT Type III	1	M	62	Frontal cortex
AGD	1	M	90	Nucleus accumbens
	2	M	85	Nucleus accumbens
ARTAG	1	F	85	Hippocampus
MAPT intron 10 mutation (+3)	1	F	54	Frontal cortex
	2	F	63	Frontal cortex
MAPT intron 10 mutation (+16)	1	M	53	Frontal cortex
FBD	1	F	68	Hippocampus
FDD	1	M	52	Temporal cortex

nature research

Corresponding author(s): Michel Goedert, Sjors H.W. Scheres

Last updated by author(s): Jul 30, 2021

Reporting Summary

Nature Research wishes to improve the reproducibility of the work that we publish. This form provides structure for consistency and transparency in reporting. For further information on Nature Research policies, see our Editorial Policies and the Editorial Policy Checklist.

Statistics

For all statistical analyses, confirm that the following items are present in the figure legend, table legend, main text, or Methods section.

n/a	Confirmed	
☐	☒	The exact sample size (*n*) for each experimental group/condition, given as a discrete number and unit of measurement
☐	☒	A statement on whether measurements were taken from distinct samples or whether the same sample was measured repeatedly
☒	☐	The statistical test(s) used AND whether they are one- or two-sided *Only common tests should be described solely by name; describe more complex techniques in the Methods section.*
☒	☐	A description of all covariates tested
☒	☐	A description of any assumptions or corrections, such as tests of normality and adjustment for multiple comparisons
☒	☐	A full description of the statistical parameters including central tendency (e.g. means) or other basic estimates (e.g. regression coefficient) AND variation (e.g. standard deviation) or associated estimates of uncertainty (e.g. confidence intervals)
☒	☐	For null hypothesis testing, the test statistic (e.g. F, t, r) with confidence intervals, effect sizes, degrees of freedom and P value noted *Give P values as exact values whenever suitable.*
☒	☐	For Bayesian analysis, information on the choice of priors and Markov chain Monte Carlo settings
☒	☐	For hierarchical and complex designs, identification of the appropriate level for tests and full reporting of outcomes
☒	☐	Estimates of effect sizes (e.g. Cohen's *d*, Pearson's *r*), indicating how they were calculated

Our web collection on statistics for biologists contains articles on many of the points above.

Software and code

Policy information about availability of computer code

Data collection	EPU (v1.11.1 and v2.3.079)
Data analysis	RELION (v3.1 and v4.0), CTFFIND (v4.1), COOT (v0.9), REFMAC (v5.8.0256), PHENIX (v1.19.2-4158), Pymol (v2.3.2 and v2.4.1), ChimeraX (v1.0), crYOLO (v1.7.5)

For manuscripts utilizing custom algorithms or software that are central to the research but not yet described in published literature, software must be made available to editors and reviewers. We strongly encourage code deposition in a community repository (e.g. GitHub). See the Nature Research guidelines for submitting code & software for further information.

Data

Policy information about availability of data

All manuscripts must include a data availability statement. This statement should provide the following information, where applicable:
- Accession codes, unique identifiers, or web links for publicly available datasets
- A list of figures that have associated raw data
- A description of any restrictions on data availability

Cryo-EM maps have been deposited in the Electron Microscopy Data Bank (EMDB) under accession numbers EMD-13218 for PSP, EMD-13219 for GGT type 1, EMD-13220 for GGT type 2, EMD-13221 for GGT type 3, EMD-13223 for GPT type 1a, EMD-13224 for GPT type 1b, EMD-13225 for GPT type 2, EMD-13226 for AGD type 1 and EMD-13227 for AGD type 2. Corresponding refined atomic models have been deposited in the Protein Data Bank (PDB) under accession numbers 7P65 for PSP, 7P66 for GGT type 1, 7P67 for GGT type 2, 7P68 for GGT type 3, 7P6A for GPT type 1a, 7P6B for GPT type 1b, 7P6C for GPT type 2, 7P6D for AGD type 1 and 7P6E for AGD type 2. Cryo-EM raw data sets have been deposited in Electron Microscopy Public Image Archive (EMPIAR) under accession numbers 10765 for PSP-RS case 1, 10766 for GGT-I case, 10767 for PSP-F case 2, 10768 for AGD case 1, and 10769 for +16 case. Any other relevant data are available from the corresponding authors upon request.

Field-specific reporting

Please select the one below that is the best fit for your research. If you are not sure, read the appropriate sections before making your selection.

☒ Life sciences ☐ Behavioural & social sciences ☐ Ecological, evolutionary & environmental sciences

For a reference copy of the document with all sections, see nature.com/documents/nr-reporting-summary-flat.pdf

Life sciences study design

All studies must disclose on these points even when the disclosure is negative.

Sample size	Frontal cortex from PSP-RS case 1, PSP-RS case 2, PSP-P, PSP-CBS, GGT-I, GGT-II, GGT-III, +3 case 1, +3 case 2, +16, temporal cortex from PSP-F case 2, FDD, entorhinal cortex from PSP-RS case 3, hippocampus from FBD, ARTAG, putamen from PSP-F case 1, thalamus from PSP-RS case 3 and nucleus accumbens from AGD cases 1 and 2. All these samples were chosen based on availability of tissue (maximum available sample size).
Data exclusions	Pre-established common image classification procedures (S.H.W. Scheres, J. Struc. Biol. 180: 519-530, (2012)) were employed to select particle images with the highest resolution content in the cryo-EM reconstruction process. Details of the number of selected images are given in Extended Data Tables 1-4.
Replication	Depending on availability of brain tissues, we replicated our experiments as described in the main text: we performed histology and cryo-EM for 7 individuals diagnosed with PSP, 3 with GGT, 2 with AGD, 1 with ARTAG, 3 with +3/+16 mutations, 1 with FBD and 1 with FDD.
Randomization	Randomisation was not performed, as it would not reduce any bias in this study, where samples are limited by brain availability.
Blinding	Blinding was not performed, as the perceived risk of detection/performance bias was deemed negligible.

Reporting for specific materials, systems and methods

We require information from authors about some types of materials, experimental systems and methods used in many studies. Here, indicate whether each material, system or method listed is relevant to your study. If you are not sure if a list item applies to your research, read the appropriate section before selecting a response.

Materials & experimental systems

n/a	Involved in the study
☐	☒ Antibodies
☒	☐ Eukaryotic cell lines
☒	☐ Palaeontology and archaeology
☒	☐ Animals and other organisms
☐	☒ Human research participants
☒	☐ Clinical data
☒	☐ Dual use research of concern

Methods

n/a	Involved in the study
☒	☐ ChIP-seq
☒	☐ Flow cytometry
☒	☐ MRI-based neuroimaging

Antibodies

Antibodies used	For histology and immunohistochemistry, primary antibodies were: RD3 (Specific for 3R tau) (Merck Millipore, catalog number: 05-803) (1:1,000); RD4 (Specific for 4R tau) (Merck Millipore, catalog number: 05-804) (1:1,000); AT8 (specific for pS202/pT205 tau) (Thermo Fisher, catalog number: MN1020) (1:300). For Immunobloting, the primary antibody was T46 (specific for tau) (Thermo Fisher, catalog number: 13-6400) used at 1:2000.
Validation	RD3 and RD4 validated against human 3R and 4R tau, respectively in (De Silva, R. et al. Neuropathol. Appl. Neurobiol. 29:288-302 (2003)) and in manufacturer's datasheet (Millipore); AT8 validated against pS202/pT205 tau in (Mercken, M. et al. Acta Neuropathol. 84:265-272 (1992)) and in manufacturer's datasheet (Thermo Fisher); T46 validated against C-terminal region (404-441aa) of human tau in (Kosik, K. S. et al. Neuron 1(9):817-825 (1988)) and in manufacturer's datasheet (Thermo Fisher).

Human research participants

Policy information about studies involving human research participants

Population characteristics	See Methods section. Seven individuals with PSP, one individual with GGT-I, one individual with GGT-II, one individual with GGT-III, two individuals with AGD, one individual with ARTAG, two individuals with mutation +3 in intron 10 of MAPT, one individual with mutation +16 in intron 10 of MAPT, one individual with familial British dementia and one individual with familial Danish dementia. With the exception of the cases with +3 and +16 mutations, the sequences of the MAPT exons and

the adjacent introns were wild-type. PSP-RS case 1 was in an 83-year-old man; PSP-RS case 2 was in a 70-year-old man;PSP-RS case 3 was in a 74-year-old man;PSP-F case 1 was in a 62-year-old man;PSP-F case 2 was in a 66-year-old woman;PSP-P was in a 63-year-old man;PSP-CBS was in an 88-year-old woman; GGT-I was in a 77-year-old woman; GGT-II was in a 76-year-old woman;GGT-III was in a 62-year-old man; AGD case 1 was in a 90-year-old man; AGD case 2 was in an 85-year-old man; ARTAG case was in an 85-year-old woman; +3 case 1 was a 54-year old woman; +3 case 2 was in a 63-year-old woman; +16 case was in a 53-year-old man; FBD case was in a 68-year-old woman; FDD was in a 52-year-old man.

| Recruitment | Samples were selected based on brain tissue availability and post-mortem neurohistological examination, which is unlikely to have impacted the results. |

| Ethics oversight | The studies carried out at Tokyo Metropolitan Institute of Medical Science, Indiana University, UCL Queen Square Institute of Neurology, and the University of Toronto were approved by the ethics committees and through the ethical review processes at each Institution. Informed consent was obtained from the patients' next of kin. |

Note that full information on the approval of the study protocol must also be provided in the manuscript.